AIAA JOURNAL
Vol. 53, No. 2, February 2015

Three-Degree-of-Freedom Hybrid Piezoelectric-Inductive Aeroelastic Energy Harvester Exploiting a Control Surface

J. A. C. Dias* and C. De Marqui Jr.†
University of Sao Paulo, 13566-590 São Carlos, Brazil
and
A. Erturk‡
Georgia Institute of Technology, Atlanta, Georgia 30332-0405

DOI: 10.2514/1.J053108

Aeroelastic energy harvesting by transforming wind energy into low-power electricity via low-profile and geometrically scalable devices has received growing attention in the literature of energy harvesting for wireless electronic components. The goal is to harvest flow energy available in high-wind areas toward enabling self-powered systems, such as sensor networks employed in structural health and usage monitoring of aircraft and rotorcraft. Other than bluff-body-based energy harvester configurations using vortex-induced vibrations, the use of an aeroelastic typical section with a proper transduction mechanism is a popular and convenient approach to create instabilities and persistent oscillations for flow energy harvesting. In this work, a hybrid three-degree-of-freedom airfoil-based aeroelastic energy harvester that simultaneously uses piezoelectric transduction and electromagnetic induction is analyzed based on fully coupled electroaeroelastic modeling. This particular configuration exploits a control surface for enhanced design flexibility as compared to its well-explored two-degree-of-freedom counterparts. The two transduction mechanisms are added to the plunge degree of freedom in the presence of two separate electrical loads, and dimensionless electroaeroelastic equations are obtained. The effects of aeroelastic parameters and load resistance values on the overall electroaeroelastic behavior (total power generation and linear flutter speed) are discussed in detail.

Nomenclature

a	=	distance from the semichord (chordwise geometric midpoint) to the elastic axis, m
$\mathbf{B}$	=	structural damping matrix
$\mathbf{B}_{\mathrm{nc}}$	=	noncirculatory aerodynamic matrix related to damping
b	=	semichord length of the airfoil section, m
C_p^{eq}	=	equivalent internal capacitance of the piezoceramic layers, F
c	=	distance from the semichord to the control surface elastic axis, m
d_h	=	damping coefficient per length in the plunge degree of freedom, $\mathrm{N \cdot s/m^2}$
d_α	=	damping coefficient per length in the pitch degree of freedom, $\mathrm{N \cdot s/rad}$
d_β	=	damping coefficient per length in the control surface pitch degree of freedom, $\mathrm{N \cdot s/rad}$
h	=	plunge displacement, m
$\bar{h}$	=	dimensionless plunge displacement
I	=	electromagnetically induced electric current, A
I_α	=	airfoil moment of inertia per length, $\mathrm{N \cdot m}$
I_β	=	control surface moment of inertia per length, $\mathrm{N \cdot m}$
$\bar{I}$	=	dimensionless electromagnetically induced electric current
I^*	=	reference electromagnetically induced electric current, A
$\mathbf{K}$	=	structural stiffness matrix
$\mathbf{K}_{\mathrm{nc}}$	=	noncirculatory aerodynamic matrix related to stiffness
k_h	=	stiffness per length in the plunge degree of freedom, $\mathrm{N/m^2}$
k_α	=	stiffness per length in the pitch degree of freedom, N/rad
k_β	=	stiffness per length in the control surface pitch degree of freedom, N/rad
L	=	aerodynamic lift per length (in the span direction), N/m
L_c	=	coil inductance, H
$\bar{L}$	=	dimensionless aerodynamic lift per length
l	=	span length, m
$\mathbf{M}$	=	structural mass matrix
$\mathbf{M}_{\mathrm{nc}}$	=	noncirculatory aerodynamic matrix related to inertia
M_α	=	aerodynamic moment per length, N
M_β	=	aerodynamic moment per length due to control surface, N
$\bar{M}_\alpha$	=	dimensionless aerodynamic moment per length
$\bar{M}_\beta$	=	dimensionless aerodynamic moment per length due to control surface
m	=	airfoil mass per length, kg
m_e	=	effective fixture mass (connecting the airfoil to the plunge) per length, kg
$\bar{m}$	=	dimensionless mass ratio
$\bar{P}$	=	dimensionless total electrical power output
R_c	=	internal resistance of the induction coil [Ω]
R_l^i	=	load resistance in the inductive energy-harvesting circuit [Ω]
R_l^p	=	load resistance in the piezoelectric energy-harvesting circuit [Ω]
$\bar{r}_\alpha$	=	dimensionless radius of gyration
$\bar{r}_\beta$	=	dimensionless control surface radius of gyration
t	=	time, s

Presented as Paper 2013-1795 at the 54th AIAA/ASME/ASCE/AHS/ASC Structures, Structural Dynamics, and Materials Conference, Boston, MA, 8–11 April 2013; received 15 October 2013; revision received 4 June 2014; accepted for publication 8 June 2014; published online 12 September 2014.

*Graduate Student, Department of Aeronautical Engineering, Engineering School of Sao Carlos; jose.dias@usp.br.

†Assistant Professor, Department of Aeronautical Engineering, Engineering School of Sao Carlos; demarqui@sc.usp.br.

‡Assistant Professor, G. W. Woodruff School of Mechanical Engineering; alper.erturk@me.gatech.edu.

U = airflow speed, m/s
$\bar{U}$ = dimensionless airflow speed
x_α = dimensionless chordwise offset of the elastic axis from the centroid
x_β = dimensionless chordwise offset of the control surface elastic axis from the centroid of the control surface
α = pitch displacement, deg
$\bar{\alpha}$ = dimensionless pitch displacement
α^* = reference pitch angle, deg
$\underset{\sim}{\beta}$ = angular displacement of control surface, deg
β = dimensionless angular displacement of control surface
β^* = reference control surface pitch angle, deg
γ_α = pitch-to-plunge frequency ratio
γ_β = control surface pitch-to-plunge frequency ratio
ζ_h = dimensionless plunge damping factor
ζ_α = dimensionless pitch damping factor
ζ_β = dimensionless control surface pitch damping factor
η = dimensionless equivalent piezoelectric capacitance
θ = piezoelectric coupling, $\mathrm{A \cdot s/m}$
κ = dimensionless piezoelectric coupling
λ_c = dimensionless internal resistance of the coil
λ_l^i = dimensionless load resistance for the inductive energy-harvesting circuit
λ_l^p = dimensionless load resistance for the piezoelectric energy-harvesting circuit
$(\lambda_l^i)_{\mathrm{optimal}}$ = optimal dimensionless load resistance for the inductive energy-harvesting circuit that generates maximum power output
$(\lambda_l^p)_{\mathrm{optimal}}$ = optimal dimensionless load resistance for the piezoelectric energy-harvesting circuit that generates maximum power output
v = piezoelectric voltage output, V
$\bar{v}$ = dimensionless piezoelectric voltage output
v^* = reference voltage, V
ρ = mass density of air, $\mathrm{kg/m^3}$
τ = dimensionless time
φ = dimensionless inductance
χ = dimensionless inductive coupling
ψ = electromagnetic coupling, $\mathrm{H \cdot A/m}$
ω_h = plunge natural frequency, Hz
ω_α = pitch natural frequency, Hz
ω_β = control surface pitch natural frequency, Hz

I. Introduction

RESEARCH efforts in the field of aeroelastic energy harvesting aim to enable geometrically scalable and low-profile flow energy harvesters in order to power small electronic components for applications ranging from health monitoring in aircraft and rotorcraft structures to wireless sensors located in numerous other high-wind areas. Over the past few years, the combination of aeroelastic vibrations with an appropriate transduction mechanism for transforming wind energy into low-power electricity has received growing attention in the energy-harvesting literature. The implementations of bluff-body-based and airfoil-based configurations are two convenient ways to create persistent oscillations for flow energy harvesting [1].

An early implementation of a piezoelectric interface in flow energy harvesting appears to be the bluff-body/polyvinylidene fluoride (PVDF) membrane configuration tested under water by Allen and Smits [2], as reported in their 2001 paper. In that configuration, a von Kármán vortex street formed behind the bluff body excited the piezoelectric PVDF to extract electricity from flow-induced vibrations through the direct piezoelectric effect. For a few years following this early work, the flow energy-harvesting problem was not researched as heavily as the harvesting of direct vibrational and kinetic energy [3,4]. The literature shows that flow energy-harvesting research regained attention with an increased momentum in the past five years. For the piezoaeroelastic problem of energy harvesting from airflow excitation of a cantilevered plate with embedded piezoceramics, De Marqui et al. [5,6] presented finite element models based on the vortex-lattice method [5] and the doublet-lattice method [6] of aeroelasticity [7,8]. Time-domain simulations [5] were given for a cantilevered plate with embedded piezoceramics for various airflow speeds below the linear flutter speed and at the flutter boundary. Frequency-domain simulations [6] considering resistive and resistive-reactive shunt circuits were also presented, focusing on the linear response at the flutter boundary. Bryant and Garcia [9] studied the aeroelastic energy-harvesting problem for a two-degree-of-freedom (2-DOF) typical section by using the finite state theory of Peters et al. [10], whereas Erturk et al. [11] presented an experimentally validated lumped-parameter model for a wing section (airfoil) with piezoceramics attached onto plunge stiffness members using Theodorsen's unsteady aerodynamic model [12]. Piezoelectric power generation at the flutter boundary and its minor effect on the linear flutter speed were discussed [11]. Sousa et al. [13] investigated the nonlinear version of the same experimental setup [with a free play in the pitch degree of freedom (DOF)] to increase the operating envelope of the aeroelastic energy harvester. In a numerical case study, hardening cubic nonlinearity and free play were combined to keep the oscillation amplitudes at an acceptable level over a range of airflow speeds while reducing the cut-in speed. The exploitation of benign and detrimental nonlinearities [14,15] in energy harvesting was successfully demonstrated. Specifically, it was pointed out [11] and demonstrated [13] that the sources of catastrophic nonlinearities (such as loose joints) [14,15] (which are detrimental to real aircraft) can be used in the energy-harvesting problem for reducing the cut-in speed and increasing the power output.

The recent literature of energy harvesting shows that the interest in nonlinear aeroelastic systems for wind energy harvesting has further increased [16–19]. Bae and Inman [16] investigated the piezoaeroelastic behavior of a 2-DOF typical section with free play and cubic nonlinearity separately in the pitch DOF. The effect of pitch-to-plunge frequency ratio on the nonlinear aeroelastic behavior is discussed as well as the use of stable limit-cycle oscillations for wind energy harvesting. In an experimental investigation, Abdelkefi et al. [17] showed that the cut-in speed of subcritical instability decreases with increasing free play gap of an airfoil section. Abdelkefi et al. [18] exploited the nonlinear piezoaeroelastic behavior of wind energy harvesting, avoiding subcritical Hopf bifurcations, and presented [19] a comprehensive nonlinear analysis of piezoaeroelastic wind energy harvesters.

As an alternative to airfoil-based and cantilevered wing-based configurations, St. Clair et al. [20] presented a design that uses a piezoelectric beam embedded within a cavity under airflow. Vortex-induced oscillations of piezoelectric cantilevers located behind bluff bodies were investigated by Pobering et al. [21] and Akaydin et al. [22,23] through experiments and numerical simulations. Underwater base excitation of piezoelectric [24] and ionic polymer–metal composite [25] cantilevers has also been investigated for low-power electricity generation.

A detailed numerical analysis of the energy-harvesting potential for a foil-damper system was presented by Peng and Zhu [26] using a Navier–Stokes solution without focusing on a specific transduction mechanism. Akcabay and Young [27] investigated the energy-harvesting potential of flexible beams in viscous flow along with the effects of system parameters. Tang et al. [28] presented a rigorous analysis of the energy transfer from fluid to structure for self-excited vibrations under axial flow over a cantilever. Piezoelectric energy harvesting from limit-cycle oscillations under axial flow over a cantilever beam has also been discussed by Dunnmon et al. [29] recently. Kwon [30] considered a T-shaped cantilever beam that causes vortex-induced vibration of a cantilever in response to axial flow. Kwuimy et al. [31] employed a bistable energy harvester [32] for turbulent wind energy harvesting. Recent efforts have also employed electromagnetic induction for converting aeroelastic vibrations into electricity through flutter wake galloping [33] and bluff-body-based oscillations [34]. In addition to these recent efforts, it is worth adding that the wingmill concept employing aeroelastic vibrations was investigated previously for rather large-scale configurations as an alternative to conventional windmills and wind turbines [35–37], whereas the present research is focused on low-power electricity generation via geometrically scalable energy conversion mechanisms.

Both piezoelectric transduction and electromagnetic induction techniques have peculiar advantages in energy harvesting from flow-induced vibrations. Piezoelectric transduction is a convenient way to extract energy from structural deformations by means of attaching piezoceramic patches, whereas electromagnetic induction is useful for extracting kinetic energy from relative motions via coil-magnet arrangements based on Faraday's law. For instance, plunge DOF springs made of elastic cantilevers are sources of strain energy for piezoelectric transduction, whereas the translation at the tip of plunge spring members, or rotation of the shaft in the pitch DOF, can be exploited for inductive energy harvesting. As recently suggested with a focus on a 2-DOF aeroelastic energy harvester configuration [38], proper combination of these transduction mechanisms within a single hybrid flow energy harvester can improve the power density while employing the same simple platform. In the present work, a three-DOF (3-DOF) aeroelastic energy harvester that exploits a control surface along with piezoelectric transduction and electromagnetic induction mechanisms is analyzed based on fully coupled electroaeroelastic modeling. Both forms of electromechanical coupling are introduced to the plunge DOF. The interaction between total power generation (from piezoelectric transduction and electromagnetic induction) and the linear electroaeroelastic behavior of the typical section is investigated in the presence of two separate electrical loads. Dimensionless electroaeroelastic equations are obtained to study the effects of major design parameters and geometric scaling of the 3-DOF hybrid piezoelectric-inductive energy harvester. Several case studies are given to explore the coupled system dynamics in dimensionless parameter space and comparisons against the 2-DOF counterpart are also presented.

II. 3-DOF Typical Section with Electromechanical Coupling

A. Conventional 3-DOF Typical Section with a Control Surface

Figure 1 shows the schematic of a 3-DOF aeroelastic typical section in the absence of electromechanical coupling. The plunge, pitch, and control surface displacement variables are denoted by h, α, and β, respectively. The plunge displacement is measured at the elastic axis (positive downward), the pitch angle is measured about the elastic axis (positive clockwise), and the control surface pitch angle is measured about the control surface elastic axis (positive clockwise). In addition, b is the semichord length of the airfoil section, a is the distance from the semichord (chordwise geometric midpoint) to the elastic axis, c is the distance from the semichord to the control surface elastic axis, x_α is the dimensionless chordwise offset of the elastic axis from the centroid, x_β is the dimensionless chordwise offset of the control surface elastic axis from the elastic axis of the control surface, k_h is the stiffness per length in the plunge DOF, k_α is the stiffness per length in the pitch DOF, k_β is the stiffness per length in the control surface pitch DOF, d_h is the damping coefficient per length in the plunge DOF, d_α is the damping coefficient per length in the pitch DOF, d_β is the damping coefficient per length in the control surface pitch DOF, and U is the airflow speed.

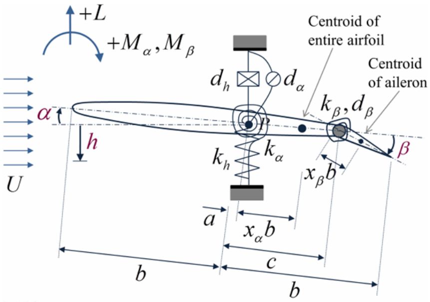

Fig. 1 Schematic of a 3-DOF aeroelastic typical section with a control surface.

The linear aeroelastic equations of an electrically uncoupled 3-DOF typical section [7,8,12] are

$$(m + m_e)\ddot{h} + mbx_\alpha\ddot{\alpha} + d_h\dot{h} + k_h h = -L \tag{1}$$

$$mbx_\alpha\ddot{h} + I_\alpha\ddot{\alpha} + (I_\beta + (c - a)mbx_\beta)\ddot{\beta} + d_\alpha\dot{\alpha} + k_\alpha\alpha = M_\alpha \tag{2}$$

$$mbx_\beta\ddot{h} + I_\beta\ddot{\beta} + (I_\alpha + (c - a)mbx_\alpha)\ddot{\alpha} + d_\beta\dot{\beta} + k_\beta\beta = M_\beta \tag{3}$$

where m is the airfoil mass per length (in the span direction), m_e is the effective fixture mass (connecting the airfoil to the plunge springs: it is zero in the ideal representation of Fig. 1) per length, I_α is the airfoil moment of inertia per unit length, I_β is the control surface moment of inertia per unit length, L is the aerodynamic lift per length, M_α is the aerodynamic moment per unit length, M_β is the aerodynamic moment per unit length due the control surface, and the overdot represents differentiation with respect to time t. The unsteady aerodynamic loads (lift and moment terms) due to arbitrary motions are obtained from Jones' approximation [39] of Wagner's indicial function [40], which is an approximation to the generalized Theodorsen function [12].

B. Electromechanically Coupled Aeroelastic Typical Section: Electroaeroelastic System

Piezoelectric transduction and electromagnetic induction are added to the plunge DOF of the typical section along with a resistive electrical load for each electrical circuit. Figure 2a shows the physical configuration of the resulting 3-DOF hybrid piezoelectric-inductive energy harvester, whereas Fig. 2b displays the lumped-element representation with additional electrical components and terms (as compared to Fig. 1). The additional parameters are the piezoelectric voltage output v (across the resistive load R_l^p) and the inductive current output I (flowing to the resistive load R_l^i).

The next sections present modeling and dimensionless analysis of the electroaeroelastic system depicted by Fig. 2. The design problem in low-power harvesting is to reduce the cut-in speed to practical values and increase the power output while keeping the device geometry small. Therefore, the focus is placed on the flutter boundary (neutral stability condition) in the following linear investigation, since the main goal is to understand the interaction between the dependence of the cut-in speed (flutter speed) and power output on various aeroelastic and electromechanical system parameters. Such a linearized approach to the problem at the flutter boundary is acceptable for the neutral stability condition of physical systems exhibiting benign nonlinearity [14,15] and supercritical postflutter bifurcation.

III. Dimensionless Electroaeroelastic Equations and Solution Method

A. Governing Equations

The electroaeroelastically coupled equations governing the dynamics of the hybrid (piezoelectric-inductive) 3-DOF aeroelastic energy harvester (Fig. 2) are

$$(m+m_e)\ddot{h}+mbx_\alpha\ddot{\alpha}+mbx_\beta\ddot{\beta}+d_h\dot{h}+k_h h-\frac{\theta}{l}v-\frac{\psi}{l}I=-L \tag{4}$$

$$mbx_\alpha\ddot{h} + I_\alpha\ddot{\alpha} + (I_\beta + (c - a)mbx_\beta)\ddot{\beta} + d_\alpha\dot{\alpha} + k_\alpha\alpha = M_\alpha \tag{5}$$

$$mbx_\beta\ddot{h} + I_\beta\ddot{\beta} + (I_\alpha + (c - a)mbx_\alpha)\ddot{\alpha} + d_\beta\dot{\beta} + k_\beta\beta = M_\beta \tag{6}$$

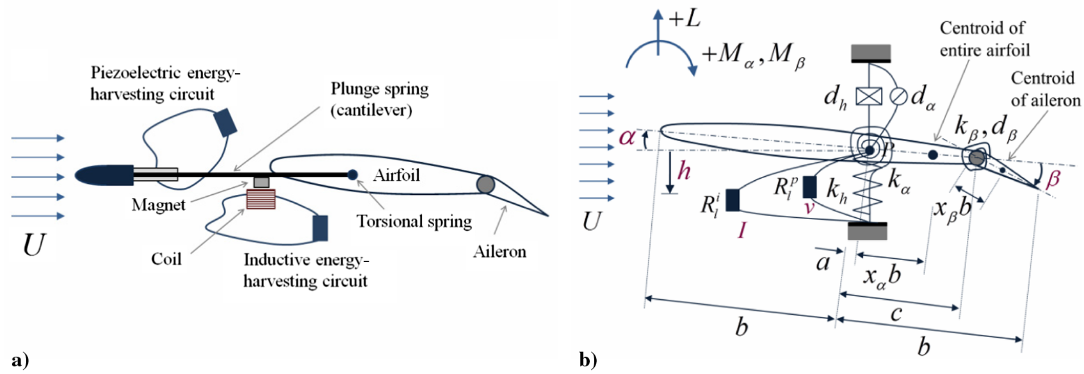

Fig. 2 Schematics of a 3-DOF hybrid piezoelectric-inductive aeroelastic energy harvester under flow excitation: a) physical system and b) lumped-element representation (mechanical degrees of freedom are h, α, and β; piezoelectric voltage output is v; and electromagnetically induced current is I).

$$C_p^{\mathrm{eq}}\dot{v} + \frac{v}{R_l^p} + \theta\dot{h} = 0 \tag{7}$$

$$L_c\dot{I} + (R_c + R_l^i)I + \psi\dot{h} = 0 \tag{8}$$

where θ is the piezoelectric coupling, ψ is the electromagnetic coupling, l is the span length, C_p^{eq} is the equivalent internal capacitance of the piezoceramic layer(s), R_l^p is the load resistance in the piezoelectric energy-harvesting circuit, v is the voltage across R_l^p, L_c is the coil inductance, R_c is the internal resistance of the inductor coil, R_l^i is the load resistance in the inductive energy-harvesting circuit, and I is the electromagnetically induced electric current flowing to R_l^i.

Equations (4–8) can be written in dimensionless form as

$$\bar{m}\bar{h}'' + x_\alpha\bar{\alpha}'' + \zeta_h\bar{h}' + \bar{h} - \kappa\bar{v} - \chi\bar{I} = -\bar{L}_h \tag{9}$$

$$x_\alpha\bar{h}'' + \bar{r}_\alpha^2\bar{\alpha}'' + \left(\bar{r}_\beta^2 + \left(\frac{c-a}{b}\right)x_\beta\right)\bar{\beta}'' + \zeta_\alpha\bar{\alpha}' + \gamma_\alpha^2\bar{r}_\alpha^2\bar{\alpha} = \bar{M}_\alpha \tag{10}$$

$$x_\beta\bar{h}'' + \bar{r}_\beta^2\bar{\beta}'' + \left(\bar{r}_\alpha^2 + \left(\frac{c-a}{b}\right)x_\alpha\right)\bar{\alpha}'' + \zeta_\beta\bar{\beta}' + \gamma_\beta^2\bar{r}_\beta^2\bar{\beta} = \bar{M}_\beta \tag{11}$$

$$\eta\bar{v}' + \frac{\bar{v}}{\lambda_l^p} + \kappa\bar{h}' = 0 \tag{12}$$

$$\varphi\bar{I}' + \lambda_c\bar{I} + \lambda_l^i\bar{I} + \chi\bar{h}' = 0 \tag{13}$$

where $\bar{m} = (m + m_e)/m$, $\bar{h} = h/b$ is the dimensionless plunge displacement, $\bar{\alpha} = \alpha/\alpha^*$ (where $\alpha^* = 1$ rad is the reference pitch angle, i.e., $\bar{\alpha} = \alpha$), $\bar{\beta} = \beta/\beta^*$ (where $\beta^* = 1$ rad is the reference control surface pitch angle, i.e., $\bar{\beta} = \beta$), $\zeta_h = d_h/m\omega_h$ is the plunge damping factor, $\zeta_\alpha = d_\alpha/mb^2\omega_h$ is the dimensionless pitch damping factor, $\zeta_\beta = d_\beta/mb^2\omega_h$ is the dimensionless control surface pitch damping factor, $\bar{r}_\alpha = r_\alpha/b$ is the dimensionless radius of gyration, $\bar{r}_\beta = r_\beta/b$ is the dimensionless control surface radius of gyration, $\bar{v} = v/v^*$ (where $v^* = 1$ V is the reference voltage for nondimensionalization), $\kappa = \theta v^*/lmb\omega_h^2$ is the dimensionless piezoelectric coupling, $\eta = C_p^{\mathrm{eq}}(v^*)^2/mb^2l\omega_h^2$ is the dimensionless equivalent capacitance, $\lambda_l^p = R_l^p mb^2l\omega_h^3/(v^*)^2$ is the dimensionless load resistance for the piezoelectric energy-harvesting circuit, $\bar{I} = I/I^*$ (where $I^* = 1$ A is the reference current), $\chi = \psi I^*/lmb\omega_h^2$ is the dimensionless inductive coupling, $\varphi = L_c(I^*)^2/lmb^2\omega_h^2$ is the dimensionless inductance, $\lambda_l^i = R_l^i(I^*)^2/lmb^2\omega_h^3$ is the dimensionless load resistance for the inductive energy-harvesting circuit, $\lambda_c = R_c(I^*)^2/lmb^2\omega_h^3$ is the dimensionless internal resistance of the induction coil, $\gamma_\alpha = \omega_\alpha/\omega_h$ is the pitch-to-plunge frequency ratio, $\gamma_\beta = \omega_\beta/\omega_h$ is the control surface pitch-to-plunge frequency ratio, $\omega_h^2 = k_h/m$ is the square of the plunge natural frequency, $\omega_\alpha^2 = k_\alpha/I_\alpha$ is the square of the pitch natural frequency, and $\omega_\beta^2 = k_\beta/I_\beta$ is the square of the control surface pitch natural frequency. The dimensionless aerodynamic loads are $\bar{L} = L/mb\omega_h^2$, $\bar{M}_\alpha = M_\alpha/mb^2\omega_h^2$, and $\bar{M}_\beta = M_\beta/mb^2\omega_h^2$. In the governing equations given by Eqs. (9–13), the prime ($'$) denotes differentiation with respect to the dimensionless time $\tau = \omega_h t$.

B. State-Space Model and Numerical Solution

The coupled piezoaeroelastic equations can be written in the state-space form by introducing electromechanical coupling to the unsteady aerodynamic model proposed by Edwards et al. [41]. The voltage and current outputs in the piezoelectric and inductive circuits, respectively, are considered as two additional state variables. The state-space electroaeroelastic equations in the matrix form are then

$$\begin{bmatrix} \mathbf{I} & \mathbf{0} & \mathbf{0} & \mathbf{0} & \mathbf{0} \\ \mathbf{0} & \tilde{\mathbf{M}} & \mathbf{0} & \mathbf{0} & \mathbf{0} \\ \mathbf{0} & \mathbf{0} & \mathbf{I} & \mathbf{0} & \mathbf{0} \\ \mathbf{0} & \mathbf{0} & \mathbf{0} & \eta & 0 \\ \mathbf{0} & \mathbf{0} & \mathbf{0} & 0 & \varphi \end{bmatrix} \begin{Bmatrix} \mathbf{x}' \\ \mathbf{x}' \\ \mathbf{x}_a' \\ \bar{v}' \\ \bar{I}' \end{Bmatrix} = \begin{bmatrix} \mathbf{0} & \mathbf{I} & \mathbf{0} & \mathbf{0} & \mathbf{0} \\ -\tilde{\mathbf{K}} & -\tilde{\mathbf{B}} & \mathbf{D} & \mathbf{\Theta}_1 & \mathbf{X}_1 \\ \mathbf{E}_1 & \mathbf{E}_2 & \mathbf{F} & \mathbf{0} & \mathbf{0} \\ \mathbf{0} & \mathbf{\Theta}_2 & \mathbf{0} & \frac{1}{\lambda_l^p} & 0 \\ \mathbf{0} & \mathbf{X}_2 & \mathbf{0} & 0 & Z \end{bmatrix} \begin{Bmatrix} \mathbf{x} \\ \mathbf{x}' \\ \mathbf{x}_a \\ v \\ \bar{I} \end{Bmatrix} \tag{14}$$

where $\mathbf{x} = \{\bar{\alpha} \quad \bar{\beta} \quad \bar{h}\}^T$, $\mathbf{\Theta}_1 = \{0 \quad 0 \quad \kappa\}^T$, $\mathbf{\Theta}_2 = \{0 \quad 0 \quad \kappa\}$, $\mathbf{X}_1 = \{0 \quad 0 \quad \chi\}^T$, $\mathbf{X}_2 = \{0 \quad 0 \quad \chi\}$, $Z = (\lambda_l^i + \lambda_c)$, $\mathbf{x}_a = \{x_1 \quad x_2 \quad x_3\}^T$ describes the three augmented aerodynamic states, $\mathbf{I}$ is the 3×3 identity matrix, and the superscript T stands for transpose. The mass, stiffness, and damping-related matrices in Eq. (14) are

$$\tilde{\mathbf{M}} = \mathbf{M} - \frac{\rho b^2}{m}\mathbf{M}_{\mathrm{nc}} \tag{15}$$

$$\tilde{\mathbf{K}} = \mathbf{K} - \frac{\rho b^2}{m}\left(\frac{U}{b}\right)^2\left(\mathbf{K}_{\mathrm{nc}} + \frac{1}{2}\mathbf{R}\mathbf{S}_1\right) \tag{16}$$

$$\tilde{\mathbf{B}} = \mathbf{B} - \frac{\rho b^2}{m}\left(\frac{U}{b}\right)\left(\mathbf{B}_{\mathrm{nc}} + \frac{1}{2}\mathbf{R}\mathbf{S}_2\right) \tag{17}$$

where $\mathbf{M}$ is the structural mass matrix, $\mathbf{B}$ is the structural damping matrix, $\mathbf{K}$ is the structural stiffness matrix, and ρ is the mass density of air. Furthermore $\mathbf{M}_{\mathrm{nc}}$, $\mathbf{B}_{\mathrm{nc}}$, and $\mathbf{K}_{\mathrm{nc}}$ are the noncirculatory aerodynamic matrices related to inertia, damping, and stiffness, respectively. These matrices, as well as the aerodynamic matrices $\mathbf{D}$, $\mathbf{E}_1$, $\mathbf{E}_2$, $\mathbf{F}$, $\mathbf{R}$, $\mathbf{S}_1$, and $\mathbf{S}_2$, can be found in Edwards et al. [41].

Table 1 Nominal properties of the aeroelastic energy harvester analyzed in this work

Parameter	Value	Unit
$\bar{m}$	2.5940	—
x_α	0.25	—
x_β	0.0204	—
$\bar{r}_\alpha$	0.5467	—
$\bar{r}_\beta$	0.1019	—
γ_α	0.5090	—
γ_β	1.949	—
ζ_h	0.0535	—
ζ_α	0.1102	—
ζ_β	0.032	—
κ	5.9×10^{-6}	—
χ	0.0229	—
η	3.66×10^{-9}	—
φ	0.0130	—
λ_c	0.1022	—
c/b	0.5	—
a/b	−0.5	—

Equation (14) can be also represented as

$$\tilde{\mathbf{x}}' = \mathbf{A}\tilde{\mathbf{x}} \tag{18}$$

where

$$\mathbf{A} = \begin{bmatrix} \mathbf{0} & \mathbf{I} & \mathbf{0} & \mathbf{0} & \mathbf{0} \\ -\tilde{\mathbf{M}}^{-1}\tilde{\mathbf{K}} & -\tilde{\mathbf{M}}^{-1}\tilde{\mathbf{B}} & \tilde{\mathbf{M}}^{-1}\mathbf{D} & \tilde{\mathbf{M}}^{-1}\mathbf{\Theta}_1 & \tilde{\mathbf{M}}^{-1}\mathbf{X}_1 \\ \mathbf{E}_1 & \mathbf{E}_2 & \mathbf{F} & \mathbf{0} & \mathbf{0} \\ \mathbf{0} & \frac{1}{\eta}\mathbf{\Theta}_2 & \mathbf{0} & \frac{1}{\eta}\frac{1}{\lambda_l^p} & 0 \\ \mathbf{0} & \frac{1}{\varphi}\mathbf{X}_2 & \mathbf{0} & 0 & \frac{1}{\varphi}Z \end{bmatrix} \tag{19}$$

$$\tilde{\mathbf{x}} = \{\mathbf{x} \quad \mathbf{x}' \quad \mathbf{x}_a \quad \bar{v} \quad \bar{I}\}^t \tag{20}$$

Next, numerical case studies are presented based on the foregoing electroaeroelastic framework and its numerical solution.

IV. Case Studies

A. Analysis Procedure and Nominal System Parameters

In the following sections, the effects of various system parameters on the dimensionless electrical power output as well as on the dimensionless linear flutter speed are investigated for the 3-DOF hybrid aeroelastic energy harvester. The optimal load resistance values for each set of parameters are identified numerically and directly employed in the simulations. The interaction between electrical power generation and linear electroaeroelastic behavior of the typical section at the flutter boundary is investigated. The effect of internal coil resistance is also discussed. The flutter speed for each set of dimensionless parameters is obtained by checking the real part of the eigenvalues of the state matrix with increasing airflow speed. The power output is obtained from the steady-state time histories at the flutter speed of each set of dimensionless parameters. The nominal properties of the aeroelastic energy harvester are given in Table 1 (the pitch and plunge DOF-related components of these parameters are based on the 2-DOF physical system explored by Sousa et al. [13]).

B. Effects of Various Aeroelastic Parameters

The effects of dimensionless radius of gyration $\bar{r}_\alpha$, pitch-to-plunge frequency ratio γ_α, control surface pitch-to-plunge frequency ratio γ_β, chordwise offset of the elastic axis from the centroid x_α, and damping ratio of each DOF on the dimensionless total electrical power output ($\bar{P} = \bar{v}^2/\lambda_l^p + \bar{I}^2\lambda_l^i$), as well as the dimensionless flutter speed $\bar{U}$ of the hybrid piezoelectric-inductive aeroelastic energy harvester, are investigated for the optimal electrical loads.

The variation of dimensionless flutter speed and total electrical power output with dimensionless $\bar{r}_\alpha$ and γ_α are displayed in Figs. 3a

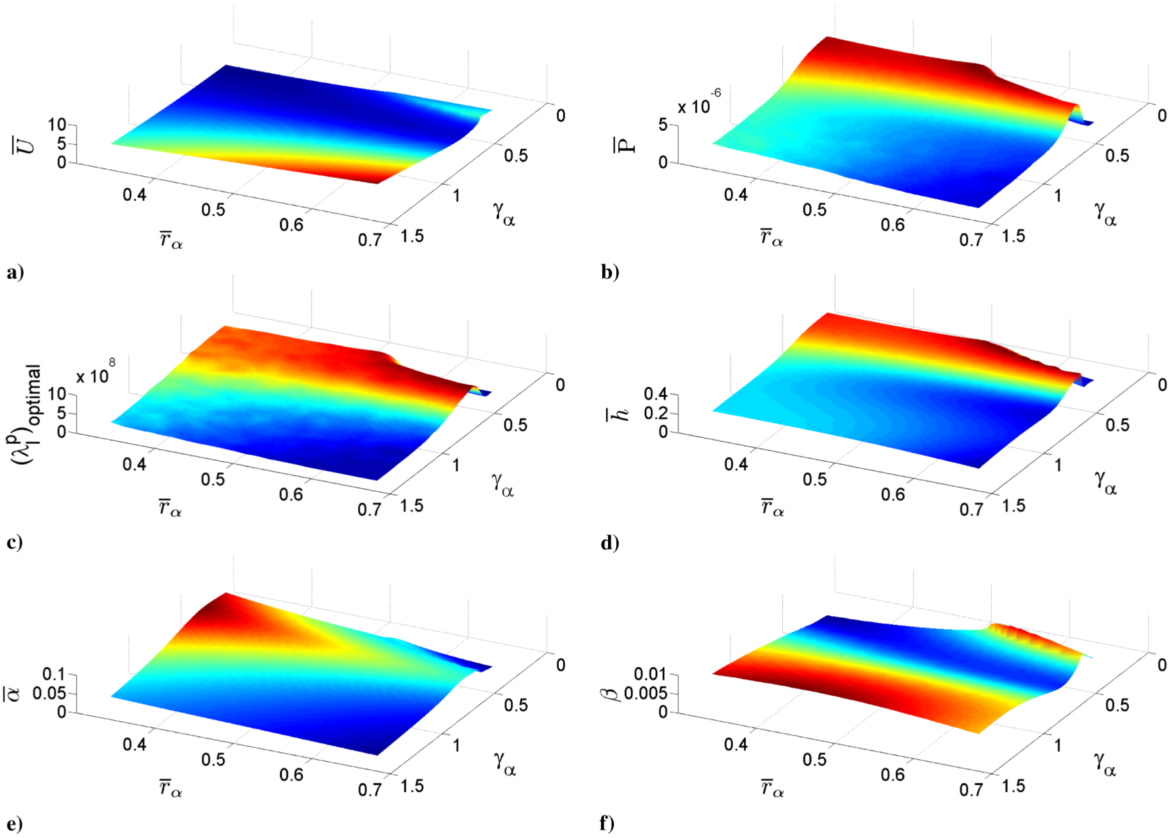

Fig. 3 Dimensionless a) flutter speed, b) total power output, c) load resistance (of the piezoelectric energy-harvesting circuit), d) plunge displacement, e) pitch displacement, and f) control surface displacement versus $\bar{r}_\alpha$ and γ_α at the flutter boundary (remaining parameters have their nominal values given in Table 1).

and 3b, respectively, for the optimal electrical load resistance values (shown in Fig. 3c) of a range of $\bar{r}_\alpha$–γ_α combinations in both circuits with fixed x_α. The simulations are specifically run for the optimal load cases to maximize the power output. The optimal dimensionless load resistance for the inductive energy-harvesting circuit that generates maximum power output remains close to the value of dimensionless internal coil resistance, $(\lambda_l^i)_{\mathrm{optimal}} \cong \lambda_c = 0.1022$, in agreement with the maximum power transfer theorem [42]. The dimensionless flutter speed remains nearly constant for small values of $\bar{r}_\alpha$ and γ_α, and it increases with the increasing dimensionless radius of gyration and pitch-to-plunge frequency ratio. The total power output shown in Fig. 3b is for the optimal electrical load values shown in Fig. 3c in this parameter space. The optimal inductive load is constant and equal to the internal coil resistance. Distinct regions can be observed for the power output in Fig. 3b. For large $\bar{r}_\alpha$ and small γ_α, the power output significantly drops. In this region, the control surface DOF β becomes unstable, whereas the plunge h and pitch α DOFs are the stable ones and they exhibit small-amplitude oscillations (Figs. 3d–3f). Since the electromechanical coupling is added to the plunge DOF, the electrical power output drops in this region of $\bar{r}_\alpha - \gamma_\alpha$ combinations (which should be avoided in design). From an alternative point of view, electromechanical coupling could be added to control surface pitch DOF to exploit the parameter combinations in this region. For the region in which the control surface is stable (roughly, for $\bar{r}_\alpha < 0.5$ and moderate-to-low γ_α values), the plunge DOF is unstable (and presents larger displacements) and power increases with decreasing γ_α for any value of $\bar{r}_\alpha$.

The variation of dimensionless flutter speed with x_α and γ_α is displayed in Fig. 4a for the optimal electrical load resistance values in both circuits and fixed dimensionless radius of gyration. Figure 4b shows the total power output versus x_α and γ_α obtained at each dimensionless flutter speed of Fig. 4a for the optimal electrical load values (of the piezoelectric energy-harvesting circuit) shown in Fig. 4c. Once again, the optimal load of the inductive energy-harvesting circuit is approximately constant and equal to the internal resistance of the coil. Figure 4b shows that the power output increases with decreasing γ_α and large values of x_α, and this favorable area also corresponds to low values of flutter speed (Fig. 4a). Note that the x_α–γ_α combinations yielding increased power are associated with large $\bar{h}$ and $\bar{\alpha}$ as displaced in Figs. 4d and 4e (specifically, $\bar{h}$ is most directly correlated to power output as expected). The power output significantly drops for relatively low values of γ_α and low values of x_α.

The surfaces of dimensionless flutter speed and power output versus γ_β and γ_α are displayed in Figs. 5a and 5b for the optimal electrical load resistance values in both circuits (for each combination of aeroelastic parameters: e.g., Fig. 5c for the piezoelectric energy-harvesting circuit) and nominal dimensionless radius of gyration and remaining parameters (Table 1). Figure 5b shows that the maximum electrical power output is obtained for small γ_α and large γ_β, and this region is also associated with large plunge and pitch displacements (Figs. 5d and 5e). The electrical power output is substantially reduced for large values of γ_α, which is due to the small amplitude of plunge DOF. In Fig. 5b, the control surface DOF (Fig. 5f) becomes unstable for small γ_α and γ_β. This set of γ_β–γ_α combinations should be avoided in the present design. The optimal load resistance for the inductive energy-harvesting circuit remains close to the internal coil resistance, whereas the optimal electrical load of the piezoelectric energy-harvesting circuit is shown in Fig. 5c for different γ_β and γ_α combinations.

The variation of dimensionless flutter speed and total electrical power output with the damping ratio of each DOF is displayed in Figs. 6a to 6f. The surfaces of dimensionless flutter speed and dimensionless power output versus ζ_h and γ_α are shown in Figs. 6a

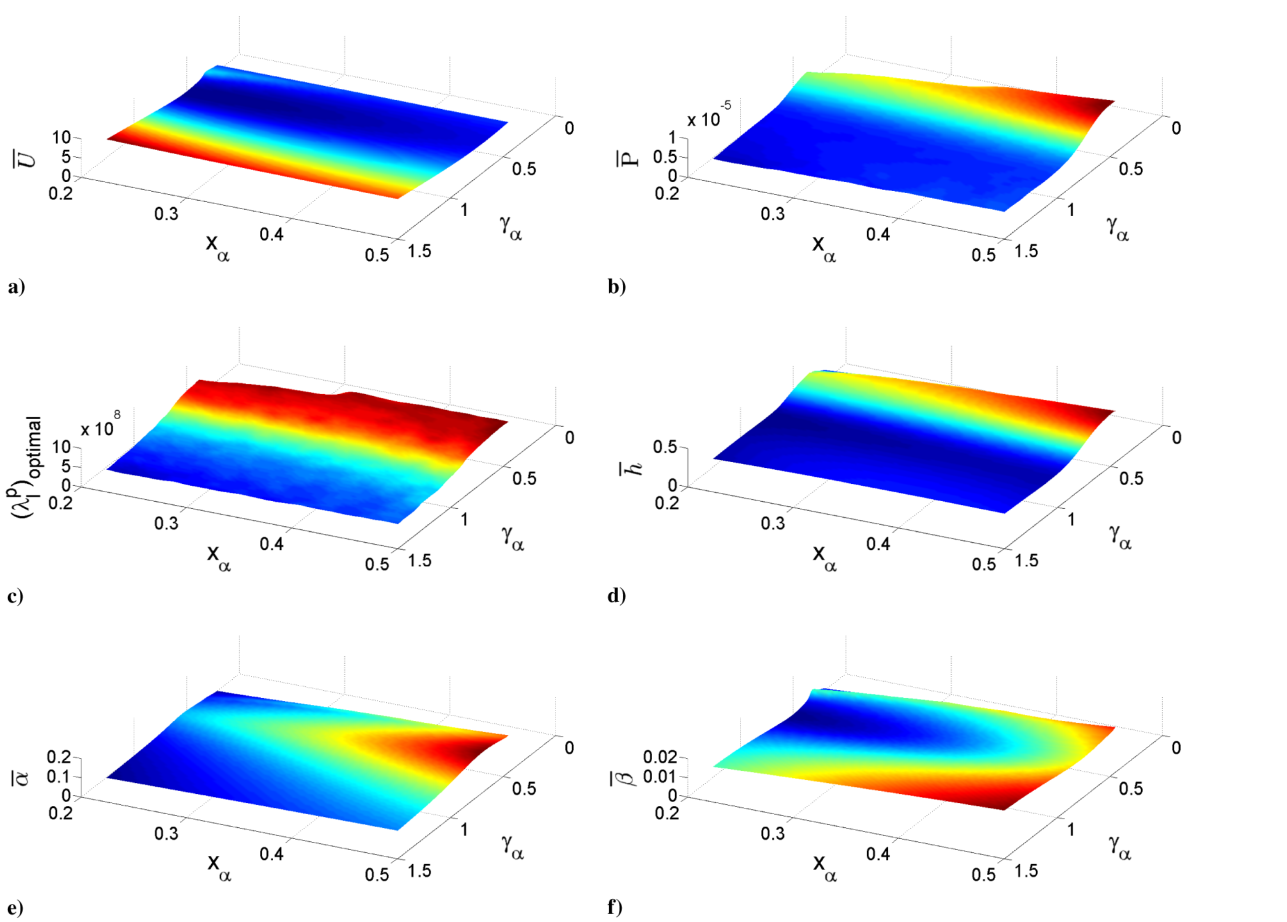

Fig. 4 **Dimensionless a) flutter speed, b) total power output, c) load resistance (of the piezoelectric energy-harvesting circuit), d) plunge displacement, e) pitch displacement, and f) control surface displacement versus x_α and γ_α at the flutter boundary (remaining parameters have their nominal values given in Table 1).**

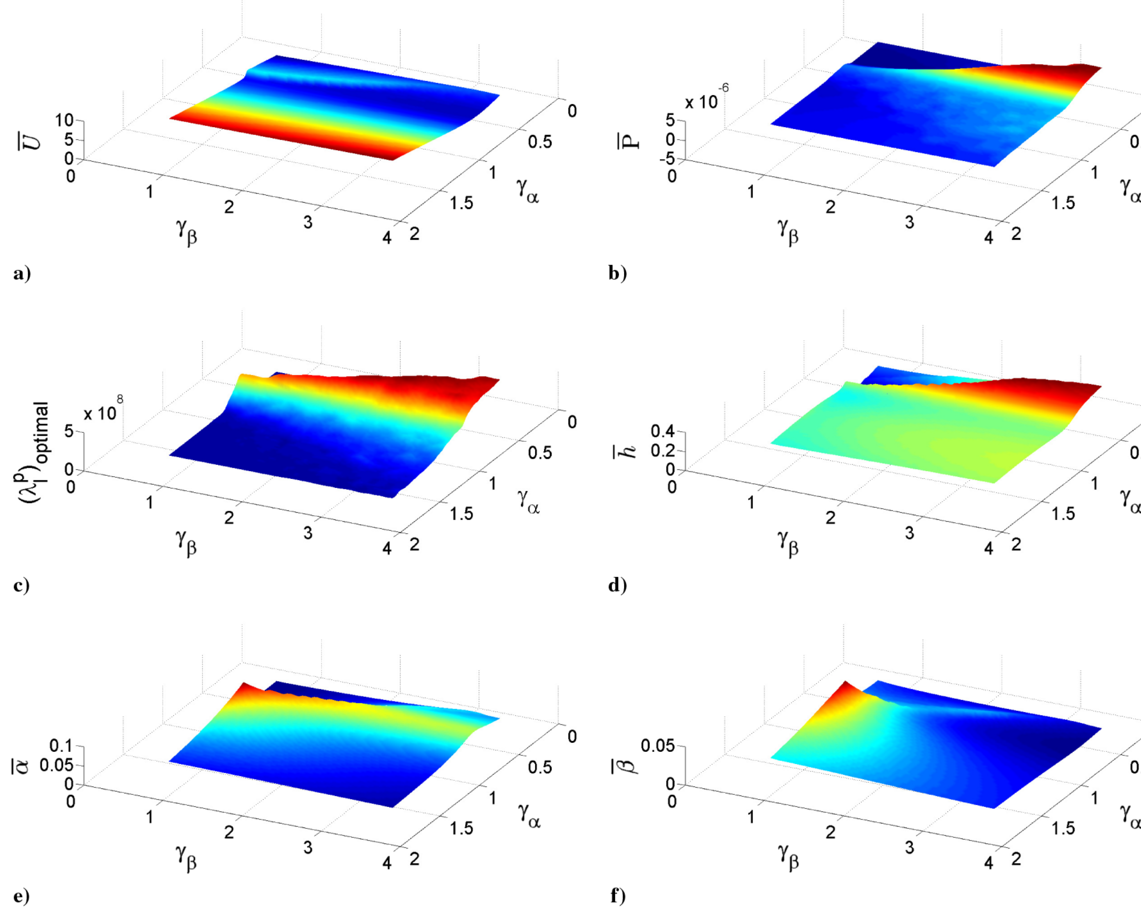

Fig. 5 Dimensionless a) flutter speed, b) total power output, c) load resistance (of the piezoelectric circuit), d) plunge displacement, e) pitch displacement, and f) control surface displacement versus γ_β and γ_α at the flutter boundary (remaining parameters have their nominal values given in Table 1).

and 6b. The flutter speed increases with increased ζ_h for $\gamma_\alpha > 1$, whereas it is insensitive to ζ_h for small values of γ_α. Although the power output increases with increased γ_α for any value of ζ_h (except the region in which plunge DOF is stable), it is insensitive to the variation of ζ_h. A similar behavior of dimensionless flutter speed and power output is observed in Figs. 6c and 6d for the variation of ζ_α and γ_α (except for small values of γ_α and large values of ζ_α where power drops). Figures 6e and 6f display the effect of ζ_β and γ_β on the dimensionless flutter speed and power output. The flutter speed increases with increased ζ_β and γ_β, whereas the dimensionless power output increases with decreased ζ_β for any value of γ_β (except for very small values of γ_β where power output drops drastically).

C. Effects of Electrical Load Resistance and Internal Coil Resistance Values

In this section, the effects of dimensionless resistive loads (in the inductive and piezoelectric energy-harvesting circuits) on dimensionless electrical power as well as flutter speed of the 3-DOF hybrid piezoelectric-inductive flow energy harvester are investigated. The ranges of resistive loads in the piezoelectric and inductive circuits cover the wide interval from short- to open-circuit conditions for each circuit. A coil with an inductance of 428 mH (yielding $\varphi = 0.0130$) and internal resistance of 175Ω (yielding $\lambda_c = 0.1022$) is assumed for the inductive circuit. The remaining system parameters are assumed to take their nominal values given in Table 1.

The interaction between total power generation (from piezoelectric transduction and electromagnetic induction) and linear electro-aeroelastic behavior of the harvester at the flutter boundary is presented in Fig. 7 for broad ranges of separate resistive loads connected to each transduction interface. The variation of the total dimensionless power output $\bar{P}$ with dimensionless load resistance values λ_l^p, λ_l^i is presented in Fig. 7a. The maximum power output is observed for the combination of the optimal load resistance values of each external circuit. The optimal load of the inductive circuit is again around the coil internal resistance ($\lambda_c = 0.1022$), in agreement with the maximum power transfer theorem [42]. The surface plot of dimensionless flutter speed $\bar{U}$ versus dimensionless resistive loads of piezoelectric and inductive energy-harvesting circuits is presented in Fig. 7b. The presence of an optimal load resistance (that gives the maximum flutter speed) for the piezoelectric energy-harvesting circuit is observed for all values of load resistance of the inductive energy-harvesting circuit. The flutter speed decreases with increasing load resistance of the inductive energy-harvesting circuit for any value of load resistance of the piezoelectric energy-harvesting circuit. The fact that the optimal load resistance of the maximum power output in the inductive circuit does not match that of the maximum flutter speed is simply a consequence of the realistic nonzero internal coil resistance assumption in the presence of nonzero coil inductance. Furthermore, it can easily be shown for vibration-based electromagnetic energy harvesters [43,44] that the short-circuit stiffness is larger than the open-circuit stiffness due to electromagnetic coupling in the presence of nonzero coil inductance.

The variations of the flutter speed and power output dramatically depend on the presence of internal coil resistance in the inductive energy-harvesting circuit. This is demonstrated next by exploring the ideal case of zero coil resistance. The power output and flutter speed surface plots versus load resistance values are presented in Fig. 8 by neglecting the internal coil resistance, i.e., by assuming $\lambda_c = 0$. An optimal load resistance for the piezoelectric energy-harvesting circuit (that gives the maximum flutter speed) is again observed for all values of load resistance of the inductive energy-harvesting circuit; this is the same behavior observed of the case with internal resistance. However, in this case ($\lambda_c = 0$), the presence of an optimal load resistance for the inductive energy-harvesting circuit (that gives the maximum flutter speed) is also observed for all values of load resistance of the piezoelectric energy-harvesting circuit. It is worth

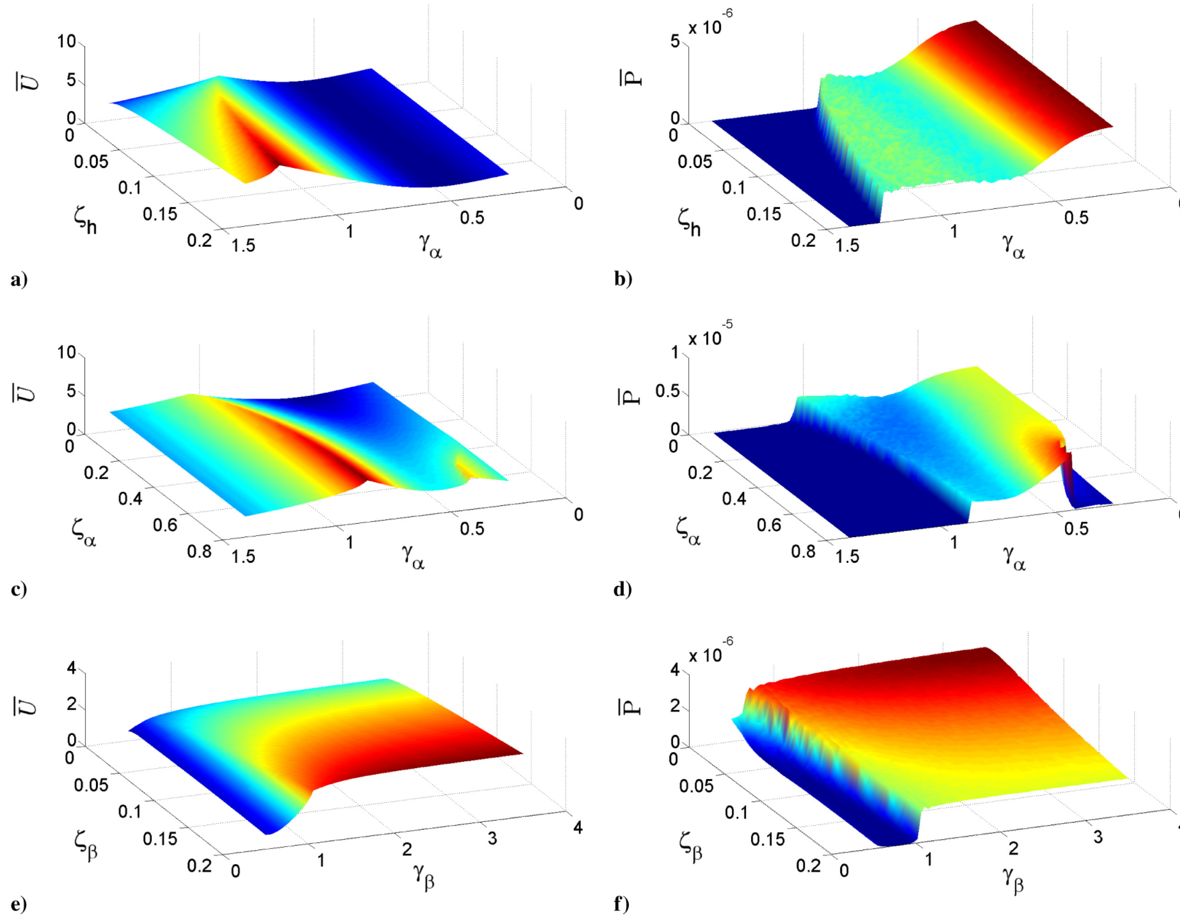

Fig. 6 Dimensionless flutter speed and total power output versus a, b) ζ_h and γ_α, c, d) ζ_α and γ_α, and e, f) ζ_β and γ_β at the flutter boundary (remaining parameters have their nominal values given in Table 1).

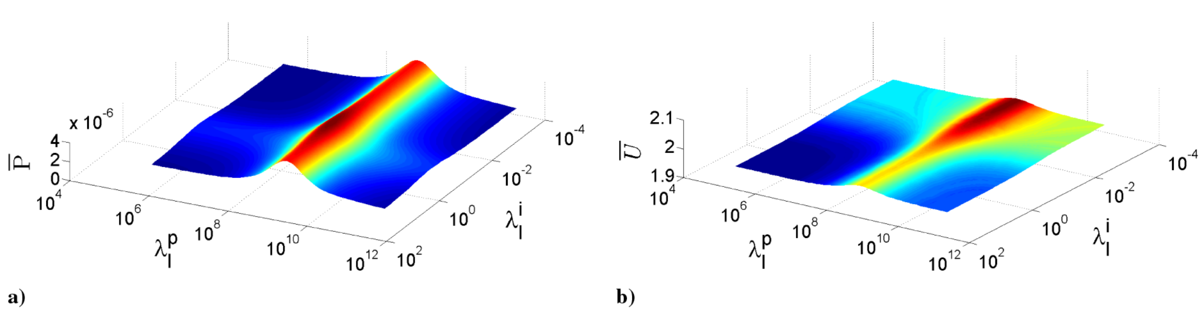

Fig. 7 Dimensionless a) total power output and b) flutter speed versus dimensionless electrical loads of both circuits (for nonzero coil resistance in the inductive circuit: $\lambda_c = 0.1022$).

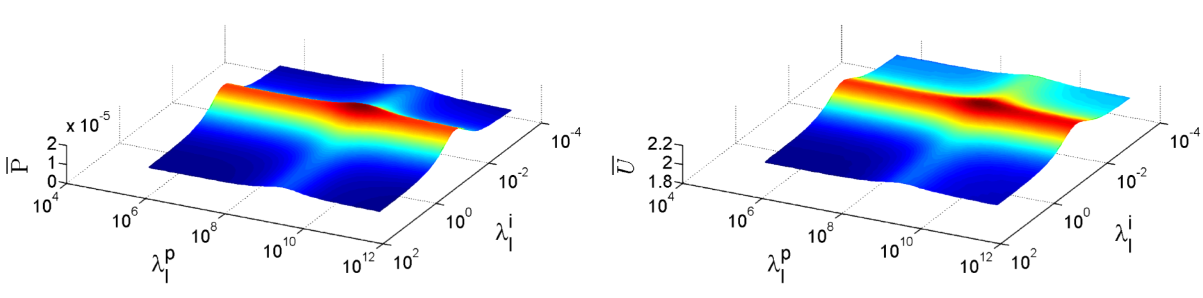

Fig. 8 Dimensionless a) total power output and b) flutter speed versus dimensionless electrical loads of both circuits (for zero coil resistance in the inductive circuit: $\lambda_c = 0$).

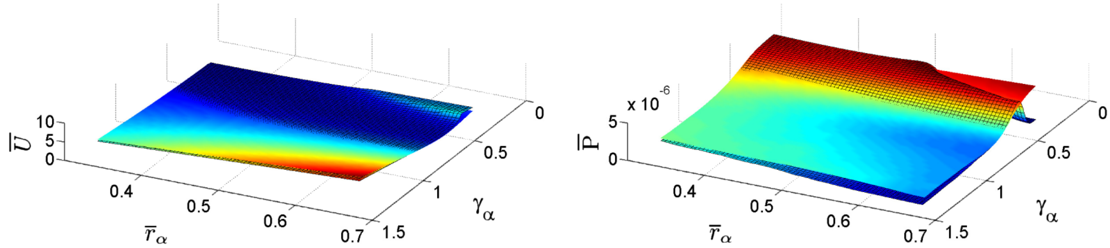

a) b)

Fig. 9 Dimensionless a) flutter speed and b) total power output versus $\bar{r}_\alpha$ and γ_α at the flutter boundary (remaining parameters have their nominal values given in Table 1 and [38]) of the 3-DOF (surface with grid) and 2-DOF harvester (surface without grid).

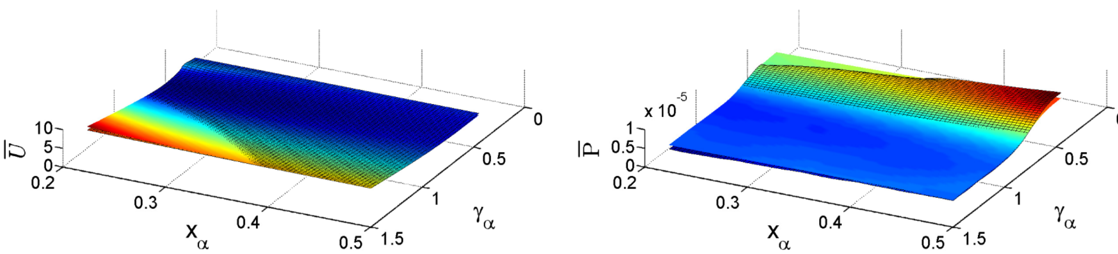

a) b)

Fig. 10 Dimensionless a) flutter speed and b) total power output versus x_α and γ_α at the flutter boundary (remaining parameters have their nominal values given in Table 1 and [38]) of the 3-DOF (surface with grid) and 2-DOF harvester (surface without grid).

adding that the exclusion of the coil resistance results in boosted power output due to reduced energy loss in the system.

D. Comparison with the 2-DOF Hybrid Aeroelastic Energy Harvester

In this section, the electroaeroelastic behavior of the 3-DOF hybrid piezoelectric-inductive harvester is compared with the electroaeroelastic behavior of the 2-DOF hybrid piezoelectric-inductive wind energy harvester [38]. The effects of the dimensionless radius of gyration $\bar{r}_\alpha$, the pitch-to-plunge frequency ratio γ_α, and the chordwise offset of the elastic axis from the centroid x_α on the dimensionless total electrical power output ($\bar{P} = \bar{v}^2/\lambda_l^p + \bar{I}^2\lambda_l^i$), as well as the dimensionless flutter speed $\bar{U}$, are investigated for the optimal electrical loads of each configuration and parameter combination.

The electroaeroelastic behavior of both harvesters is presented in Figs. 9 and 10. Figure 9a shows that flutter speed is quite similar for the 2-DOF and 3-DOF configurations; the former is slightly more preferable for small γ_α, and the latter yields lower flutter speed for large γ_α. Figure 9b shows that electrical output is enhanced in the region of small γ_α for the 3-DOF harvester, except for the region where power drops substantially (for large $\bar{r}_\alpha$ and small γ_α). The variation of dimensionless flutter speed with x_α and γ_α (Fig. 10a) is similar for the 2-DOF and 3-DOF harvesters, and the 3-DOF configuration offers slightly lower flutter speed for large γ_α and small x_α. Figure 10b shows that the maximum power output of the 3-DOF harvester is enhanced as compared to the 2-DOF case for small γ_α and large x_α. The 3-DOF harvester therefore offers the potential for improving the maximum power output with the addition of one more DOF to the design space. Further enhancements can be made by introducing electromechanical coupling to the control surface DOF.

V. Conclusions

A 3-DOF airfoil-based hybrid aeroelastic energy harvester that exploits a control surface is introduced for combined piezoelectric and inductive energy harvesting from flow excitation. The piezoelectric transduction and electromagnetic induction interfaces are added to the plunge DOF of the system. The governing aeroelastic equations are coupled with the electrical domain by taking into account two-way (feedback) interaction and considering two separate electrical loads for the hybrid energy harvester to form the resulting electroaeroelastic system. Dimensionless equations and parameters are obtained to explore the coupled system dynamics. The effects of several dimensionless system parameters (radius of gyration, chordwise offset of the elastic axis from the centroid, pitch-to-plunge frequency ratio, control surface pitch-to-plunge frequency ratio, load resistance values, and internal coil resistance) on the dimensionless electrical power output as well as the dimensionless linear flutter speed (the cut-in speed) are investigated.

It is observed that the combination of relatively large values of dimensionless offset of the elastic axis from the centroid and control surface plunge-to-pitch frequency ratio with small values of dimensionless radius of gyration and pitch-to-plunge frequency ratio favorably increases the power output while reducing the cut-in speed. It is important to note that different DOFs can become unstable for different sets of aeroelastic parameters. The electrical power output significantly drops when the plunge DOF is stable, since the electromechanical interface terms are coupled to this DOF. Further performance enhancement can be realized by considering an electromechanical coupling for the control surface pitch DOF as well to best exploit all possible instabilities associated with different aeroelastic parameters. These results and favorable parameter regions presented can be used for design and fabrication of optimal airfoil-based piezoelectric-inductive flow energy harvesters for the maximum electrical power output at reasonable airflow speeds.

In a recent paper [38], a 2-DOF hybrid piezoelectric-inductive aeroelastic energy harvester was investigated. Similar cut-in speeds were obtained from both configurations (2-DOF and 3-DOF) in the considered range of dimensionless radius of gyration, pitch-to-plunge frequency ratio, and chordwise offset for 2-DOF and 3-DOF configurations. However, larger maximum power could be extracted from the 3-DOF configuration with the proper choice of parameters. Overall, the 3-DOF configuration offers a broader design space and set of parameters to reduce the flutter speed and/or increase the maximum power output. Further enhancements can be made by introducing electromechanical coupling to the control surface DOF as well.

In all cases discussed in this work, the maximum power output is observed for the combination of the optimal load resistance values of each external circuit as expected. In the presence of internal coil resistance, the optimal load in the inductive circuit takes approximately that resistance value. The presence of an internal coil resistance affects the dimensionless flutter speed and reduces the performance of the system due to increased energy dissipation. The dimensionless flutter speed decreases with increasing load resistance in the inductive energy-harvesting circuit in the presence of coil resistance. When the internal coil resistance is neglected for the ideal lossless coil scenario, finite optimal load resistance values are obtained for the maximum flutter speed and power output.

Acknowledgments

The authors gratefully acknowledge National Council for Scientific and Technological Development (CNPq) (574001/2008-5) and Minas Gerais Research Foundation (FAPEMIG) (APQ-0076-09) for partially funding the present research work through the National Institute of Science and Technology of Smart Structures in Engineering (INCT-EIE).

References

[1] Elvin, N., and Erturk, A., *Advances in Energy Harvesting Methods*, Springer, New York, 2013.
doi:10.1007/978-1-4614-5705-3

[2] Allen, J. J., and Smits, A. J., "Energy Harvesting Eel," *Journal of Fluids and Structures*, Vol. 15, Nos. 3–4, 2001, pp. 629–640.
doi:10.1006/jfls.2000.0355

[3] Anton, S. R., and Sodano, H. A., "A Review of Power Harvesting Using Piezoelectric Materials (2003–2006)," *Smart Materials and Structures*, Vol. 16, No. 3, 2007, pp. R1–R21.
doi:10.1088/0964-1726/16/3/R01

[4] Cook-Chennault, K. A., Thambi, N., and Sastry, A. M., "Powering MEMS Portable Devices: A Review of Non-Regenerative and Regenerative Power Supply Systems with Emphasis on Piezoelectric Energy Harvesting Systems," *Smart Materials and Structures*, Vol. 17, No. 4, 2008, Paper 043001.
doi:10.1088/0964-1726/17/4/043001

[5] De Marqui, C., Jr., Erturk, A., and Inman, D. J., "Piezoaeroelastic Modeling and Analysis of a Generator Wing with Continuous and Segmented Electrodes," *Journal of Intelligent Material Systems and Structures*, Vol. 21, No. 10, 2010, pp. 983–993.
doi:10.1177/1045389X10372261

[6] De Marqui, C., Jr., Vieira, W. G. R., Erturk, A., and Inman, D. J., "Modeling and Analysis of Piezoelectric Energy Harvesting from Aeroelastic Vibrations Using the Doublet-Lattice Method," *Journal of Vibration and Acoustics*, Vol. 133, No. 1, 2010, Paper 011003.
doi:10.1115/1.4002785

[7] Bisplinghoff, R. L., and Ashley, H., *Principles of Aeroelasticity*, 1st ed., Wiley, New York, 2002.
doi:10.1016/0016-0032(62)91063-3

[8] Dowell, E. H., Curtiss, H. C., Jr., Scalan, R. H., and Sisto, F., *A Modern Course in Aeroelasticity*, 1st ed., Sijthoff and Norrdhoff, The Netherlands, 1978.
doi:10.1007/978-94-015-7858-5

[9] Bryant, M., and Garcia, E., "Modeling and Testing of a Novel Aeroelastic Flutter Energy Harvester," *Journal of Vibration and Acoustics*, Vol. 133, No. 1, 2011, Paper 011010.
doi:10.1115/1.4002788

[10] Peters, D. A., Karunamoorthy, S., and Cao, W. M., "Finite State Induced Flow Models; Part I; Two Dimensional Thin Airfoil," *Journal of Aircraft*, Vol. 32, No. 2, 1995, pp. 313–322.
doi:10.2514/3.46718

[11] Erturk, A., Vieira, W. G. R., De Marqui, C., Jr., and Inman, D. J., "On the Energy Harvesting Potential of Piezoaeroelastic Systems," *Applied Physics Letters*, Vol. 96, May 2010, Paper 184103.
doi:10.1063/1.3427405

[12] Theodorsen, T., "General Theory of Aerodynamic Instability and Mechanism of Flutter," *Langley Memorial Aeronautical Laboratory*, NACA TR-496, 1935.

[13] Sousa, V. C., Anicézio, M., De Marqui, C., Jr., and Erturk, A., "Enhanced Aeroelastic Energy Harvesting by Exploiting Combined Nonlinearities: Theory and Experiment," *Smart Materials and Structures*, Vol. 20, No. 9, Aug. 2011, Paper 094007.
doi:10.1088/0964-1726/20/9/094007

[14] Dowell, E. H., and Tang, D., "Nonlinear Aeroelasticity and Unsteady Aerodynamics," *AIAA Journal*, Vol. 40, No. 9, 2002, pp. 1697–1707.
doi:10.2514/2.1853

[15] Dowell, E. H., Edwards, J., and Strganac, T., "Nonlinear Aeroelasticity," *Journal of Aircraft*, Vol. 40, No. 5, 2003, pp. 857–874.
doi:10.2514/2.6876

[16] Bae, J. S., and Inman, D. J., "Aeroelastic Characteristics of Linear and Nonlinear Piezo-Aeroelastic Energy Harvester," *Journal of Intelligent Material Systems and Structures*, Vol. 25, No. 4, 2013, pp. 401–416.
doi:10.1177/1045389X13498312

[17] Abdelkefi, A., Nayfeh, A. H., and Hajj, M. R., "Modeling and Analysis of Piezoaeroelastic Energy Harvesters," *Nonlinear Dynamics*, Vol. 67, No. 2, 2012, pp. 925–939.
doi:10.1007/s11071-011-0035-1

[18] Abdelkefi, A., Nayfeh, A. H., and Hajj, M. R., "Design of Piezoaeroelastic Energy Harvesters," *Nonlinear Dynamics*, Vol. 68, No. 4, 2012, pp. 519–530.
doi:10.1007/s11071-011-0233-x

[19] Abdelkefi, A., and Hajj, M. R., "Performance Enhancement of Wing-Based Piezoaeroelastic Energy Harvesting Through Freeplay Nonlinearity," *Theoretical and Applied Mechanics Letters*, Vol. 3, July 2013, Paper 041001.
doi:10.1063/2.1304101

[20] Clair, D. St., Bibo, A., Sennakesavababu, V. R., Daqaq, M. F., and Li, G., "A Scalable Concept for Micropower Generation Using Flow-Induced Self-Excited Oscillations," *Applied Physics Letters*, Vol. 96, No. 14, April 2010, Paper 144103.
doi:10.1063/1.3385780

[21] Pobering, S., Ebermeyer, S., and Schwesinger, N., "Generation of Electrical Energy Using Short Piezoelectric Cantilevers in Flowing Media," *Proceedings of SPIE*, Vol. 7288, April 2009, Paper 728807.
doi:10.1117/12.815189

[22] Akaydin, H. D., Elvin, N., and Andreopoulos, Y., "Energy Harvesting from Highly Unsteady Fluid Flows using Piezoelectric Materials," *Journal of Intelligent Material Systems and Structures*, Vol. 21, No. 13, 2010, pp. 1263–1278.
doi:10.1177/1045389X10366317

[23] Akaydin, H. D., Elvin, N., and Andreopoulos, Y., "Wake of a Cylinder: A Paradigm for Energy Harvesting with Piezoelectric Materials," *Experiments in Fluids*, Vol. 49, No. 1, 2010, pp. 291–304.
doi:10.1007/s00348-010-0871-7

[24] Erturk, A., and Delporte, G., "Underwater Thrust and Power Generation using Flexible Piezoelectric Composites: An Experimental Investigation Toward Self-Powered Swimmer-Sensor Platforms," *Smart Materials and Structures*, Vol. 20, No. 12, 2011, Paper 125013.
doi:10.1088/0964-1726/20/12/125013

[25] Aureli, M., Prince, C., Porfiri, M., and Peterson, S., "Energy Harvesting from Base Excitation of Ionic Polymer Metal Composites in Fluid Environments," *Smart Materials and Structures*, Vol. 19, No. 1, 2010, Paper 015003.
doi:10.1088/0964-1726/19/1/015003

[26] Peng, Z., and Zhu, Q., "Mode Coupling and Flow Energy Harvesting by a Flapping Foil," *Physics of Fluids*, Vol. 21, No. 3, March 2009, Paper 033601.
doi:10.1063/1.3092484

[27] Akcabay, D. T., and Young, Y. L., "Hydroelastic Response and Energy Harvesting Potential of Flexible Piezoelectric Beams in Viscous Flow," *Physics of Fluids*, Vol. 24, No. 5, May 2012, Paper 054106.
doi:10.1063/1.4719704

[28] Tang, L., Paidoussis, M., and Jiang, J., "Cantilevered Flexible Plates in Axial Flow: Energy Transfer and the Concept of Flutter-Mill," *Journal of Sound and Vibration*, Vol. 326, Nos. 1–2, 2009, pp. 263–276.
doi:10.1016/j.jsv.2009.04.041

[29] Dunnmon, J. A., Stanton, S. C., Mann, B. P., and Dowell, E. H., "Power Extraction from Aeroelastic Limit Cycle Oscillations," *Journal of Fluids and Structures*, Vol. 27, No. 8, 2011, pp. 1181–1198.
doi:10.1016/j.jfluidstructs.2011.02.003

[30] Kwon, S. D., "A T-Shaped Piezoelectric Cantilever for Fluid Energy Harvesting," *Applied Physics Letters*, Vol. 97, No. 16, Oct. 2010, Paper 164102.
doi:10.1063/1.3503609

[31] Kwuimy, C. A., Litak, G., Borowiec, M., and Nataraj, C., "Performance of a Piezoelectric Energy Harvester Driven by Air Flow," *Applied Physics Letters*, Vol. 100, No. 2, Jan. 2012, Paper 024103.
doi:10.1063/1.3676272

[32] Erturk, A., Hoffmann, J., and Inman, D. J., "A Piezomagnetoelastic Structure for Broadband Vibration Energy Harvesting," *Applied Physics Letters*, Vol. 94, No. 25, June 2009, Paper 254102.
doi:10.1063/1.3159815

[33] Jung, H. J., and Lee, S. W., "The Experimental Validation of a New Energy Harvesting System Based on the Wake Galloping Phenomenon," *Smart Materials and Structures*, Vol. 20, No. 5, April 2011, Paper 055022.
doi:10.1088/0964-1726/20/5/055022

[34] Zhu, D., Beeby, S., Tudor, J., White, N., and Harris, N., "A Novel Miniature Wind Generator for Wireless Sensing Applications," *Proceedings of the IEEE Sensors Conference*, IEEE, Piscataway, NJ,

2010, pp. 1415–1418.
doi:10.1109/ICSENS.2010.5690505

[35] McKinney, W., and DeLaurier, J. D., "The Wingmill: An Oscillating-Wing Windmill," *Journal of Energy*, Vol. 5, No. 2, 1981, pp. 109–115.
doi:10.2514/3.62510

[36] Ly, K. H., and Chasteau, V. A. L., "Experiments on an Oscillating-Wing Aerofoil and Application to Wing-Energy Converters," *Journal of Energy*, Vol. 5, No. 2, 1981, pp. 116–121.
doi:10.2514/3.62511

[37] Jones, K. D., Davis, S., and Platzer, M. F., "Oscillating-Wing Power Generator," *Proceedings of the 3rd ASME/JSME Joint Fluids Engineering Conference*, FEDSM Paper 1999-7050, San Francisco, CA, July 1999.

[38] Dias, J. A. C., De Marqui, C., Jr., and Erturk, A., "Hybrid Piezoelectric-Inductive Flow Energy Harvesting and Dimensionless Electro-aeroelastic Analysis for Scaling," *Applied Physics Letters*, Vol. 102, No. 4, Jan. 2013, Paper 044101.
doi:10.1063/1.4789433

[39] Jones, R. T., "Determination of the Profile Drag of an Airplane Wing in Flight at High Reynolds Numbers," NACA TR-667, 1938.

[40] Wagner, H., "Über die Entstehung des Dynamischen Auftriebes von Tragflügeln," *ZeitschriftfürAngewandteMathematik und Mechanik*, Vol. 5, No. 1, 1925, pp. 17–35.
doi:10.1002/zamm.19250050103

[41] Edwards, J. W., Ashley, H., and Breakwell, J. V., "Unsteady Aerodynamic Modeling for Arbitrary Motions," *AIAA Journal*, Vol. 17, No. 4, 1979, pp. 593–595.
doi:10.2514/3.7348

[42] Agarwal, A., and Lang, J., *Foundations of Digital and Analog Electronic Circuits*, Morgan Kaufmann, San Francisco, CA, 2005.

[43] Amirtharajah, R., and Chandrakasan, A. P., "Self-Powered Signal Processing Using Vibration-Based Power Generation," *IEEE Journal of Solid-State Circuits*, Vol. 33, No. 5, 1998, pp. 687–695.
doi:10.1109/4.668982

[44] Elvin, N., and Elvin, A., "An Experimentally Validated Electromagnetic Energy Harvester," *Journal of Sound and Vibration*, Vol. 330, No. 10, 2011, pp. 2314–2324.
doi:10.1016/j.jsv.2010.11.024

N. Wereley
Associate Editor